Contents lists available at ScienceDirect

Energy Storage Materials

journal homepage: www.elsevier.com

Three-dimensional microsupercapacitors based on interdigitated patterns of interconnected nanowire networks

Joel Ojonugwa Omale [a], Rico Rupp [a], Pascal Van Velthem [a], Vivien Van Kerckhoven [a], Vlad-Andrei Antohe [a, b], Alexandru Vlad [a, *], Luc Piraux [a, **]

[a] Institute of Condensed Matter and Nanosciences, Université catholique de Louvain, Place Croix du Sud 1, B-1348 Louvain-la-Neuve, Belgium
[b] Research and Development Center for Materials and Electronic & Optoelectronic Devices (MDEO), Faculty of Physics, University of Bucharest, Atomiştilor Street 405, 077125 Bucharest-Măgurele, Romania

ARTICLE INFO

Article history:
Received 13 February 2019
Received in revised form 14 May 2019
Accepted 16 May 2019
Available online xxx

Keywords:
3D microsupercapacitor
Nanowire
Interdigitated
Polyaniline

ABSTRACT

There is a proliferation of autonomous microscale devices, which are increasingly in need of power sources of commensurate form factors. The trade-off between the areal energy and power capabilities of miniature energy storage devices restrict their abilities to meet the requirements of these microscale devices. Three-dimensional micro- and nanoarchitectures, however, have the potential to meet the energy requirements of autonomous microscale devices, while retaining the power capabilities of thin-film systems. In this paper, we present a novel full-cell architecture and fabrication strategy for 3D microscale energy storage devices based on template-assisted electrodeposition of three-dimensionally interconnected metallic nanowire network, and subsequent laser-patterning of the deposited nanowire network to form interdigitated electrodes. The patterned nanowire networks are functionalized with the polyaniline active electrode material via an electroless deposition procedure. We show that a footprint areal capacitance/energy enhancement of more than 5 times is achieved by just 10 μm-high nanowire networks, in addition to enhanced power capabilities.

1. Introduction

There is an increasing demand for high-performance power sources for autonomous microscale devices (microelectronic and microelectromechanical systems) [1–3]. For many of these microscale devices, high power levels, i.e., high current densities for fast discharge and recharge, for varying pulse times are intermittently required. Although microsupercapacitors are able to store less energy than microbatteries, they are far more practicable to meet the power requirements of microscale devices [4,5].

The pioneering works on microsupercapacitors (as well as microbatteries) for microscale device applications were based on a stacked configuration of thin films of the cell components (i.e., current collectors, electrodes, and solid electrolyte) [6,7]. However, these devices, in comparison to their bulk counterparts, suffered from low specific capacitance, rapid capacitance fade, and low power capabilities, which were mostly attributed to the poor ionic conductivity of the solid electrolyte. These drawbacks led to the development of microsupercapacitors with interdigitated planar electrodes having shorter inter-electrode distance, leading to improved performance, in addition to easier fabricability, and the possibility to use with all kinds of electrolytes [4,8].

While microsupercapacitors with the interdigitated configuration perform better than those with the stacked configuration, the presence of small amounts of active materials limits their areal energy storage capabilities, therefore requiring large areas to store sufficient energy to power microscale devices. To increase the areal energy, fabrication of thick-film microsupercapacitors (whether in the interdigitated or stacked configuration) is not an adequate option, since a thicker film implies longer ion- and electron-diffusion distances within the electrode material, resulting in poorer power capabilities. Consequently, there is the need for microsupercapacitors with decoupled areal energy and power capabilities to meet the requirements of microscale devices [9–12].

As with microbatteries [11,13–15], researches on decoupling the areal energy and power capabilities of microsupercapacitors have led to the development of 3D microsupercapacitors [4,9,11,16–18], which are microsupercapacitors based on 3D nanoarchitectured electrodes. By using 3D nanoarchitectures, the mass loading (i.e., the amount of material per unit area) of the electrode is increased, resulting in high areal energy storage, while retaining the nanosize required for fast ion diffusion within the electrode material.

Various architectures have been proposed for 3D microscale energy storage devices [11], but most of the reported advances for 3D microsupercapacitor electrodes centred on half-cells [9], mainly because of the difficulty in assembling full cells with 3D nanoarchitectures. More recently, advances have been reported for full-cell 3D microsupercapacitors developed by active material deposition on 3D current collecting structures, which were micro-machined by tech-

* Corresponding author.
** Corresponding author.
Email addresses: alexandru.vlad@uclouvain.be (A. Vlad); luc.piraux@uclouvain.be (L. Piraux)

https://doi.org/10.1016/j.ensm.2019.05.025
2405-8297/

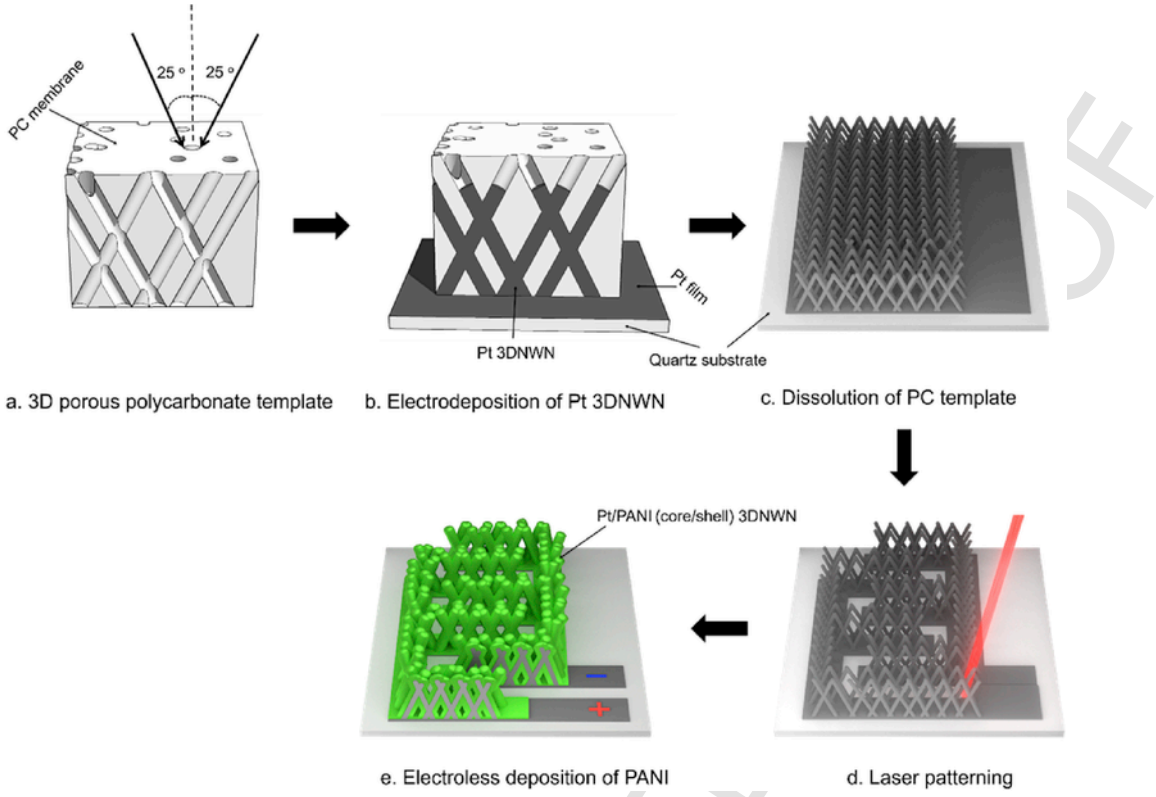

Fig. 1. Schematic of the PANI/PANI symmetrical 3D-INED microsupercapacitor fabrication process: (a) Track-etching process is used to create crossed cylindrical pores oriented at ± 25° (to the normal) in a PC membrane; (b) The resulting PC template is centred on a Cr/Pt-coated quartz substrate, after which Pt is electrodeposited through the interconnected pores of the template to form a Pt 3DNWN; (c) The electrodeposited Pt 3DNWN is then revealed by dissolution of the PC template; (d) The Pt 3DNWN, together with the Cr/Pt-coated quartz substrate, is laser-patterned to form interdigitated electrodes; (e) Finally, the Pt 3DNWN is functionalized with PANI by electroless deposition.

niques such as hydrogen bubble dynamic template synthesis [17], CO_2 laser induction [19], and high-aspect-ratio deep reactive ion etching [20]. While these approaches present impressive performances, they are all in the stacked configuration, which limits their power performances. This drawback has led to a growing interest in full-cell, 3D microsupercapacitors with the interdigitated configuration, because of the increased power performance resulting from shorter interelectrode distance, and the ease of on-chip integration, since they have both electrodes in the same plane [4,9,21]. Therefore, to simultaneously meet the energy and power requirements of microscale devices, there is need for microsupercapacitors with high-performing 3D architectures fabricated by facile techniques.

In this context, the unique architecture and high degree of interconnectivity of three-dimensionally interconnected nanowire networks (3DNWN) make them attractive nanodevice components for a wide range of applications in energy harvesting/storage systems [22–24], electronic sensing devices and actuators [25–27], magnetic and spin-caloritronic devices [28–31], catalysts [32], electrochromic elements [33], solar cells [34], biosensors [35], and bio-analytical devices [36,37]. Although self-assembled 3D nanostructures can be obtained by using chemical methods [23,38], template-assisted synthesis is the most promising route for low-cost, reliable, and large-scale fabrication of 3DNWN with controlled size, geometry, composition, and surface morphology. Typically, these nanoarchitectures are obtained by simple electrochemical deposition within hierarchical nanopores of a suitable template. So far, various 3D nanoporous templates have been used for this purpose, including silica templates [39], diblock copolymers [33], 3D alumina nanoporous hosts [22,40,41], as well as track-etched polymeric membranes [28,32]. The last is the most attractive for this purpose, as dense networks of crossed cylindrical nanopores can be obtained through sequential polycarbonate film irradiation with energetic heavy ions at different incidence angles, followed by selective chemical etching of the ion tracks within the polymer film [28]. The 3DNWN are subsequently fabricated by using a template-assisted electrochemical deposition process, followed by chemical dissolution of the polymer membrane to form macroscopic 3DNWN that are mechanically robust. In a previous work, it was shown that self-supporting 3DNWN display several advantages as electrode materials for lithium-ion batteries, thanks to the high degree of electrical connectivity and large surface area of the macroscopic sample [24].

In the present work, we developed an experimental platform that allows for the fabrication and characterization of a 3D microsupercapacitor architecture based on 3DNWN. The 3DNWN is not self-supported but is integrated on a rigid quartz chip substrate, with good adhesion between nanowires and substrates, thus providing enhanced mechanical stability of the 3DNWN films, and better potential for integration within microelectronics circuitry and devices. Using laser ablation for patterning electrodes, we successfully demonstrated the 3D interdigitated nanowire electrode design (3D-INED), which we define as a microbattery/microsupercapacitor architecture with side-by-side interdigitated electrodes, each consisting of substrate-supported metallic 3DNWN that act as scaffolds and current collectors for the electrode active materials. There are many advantages of the 3D-INED for the foreseen applications. First, by functionalizing the metallic 3DNWN with a thin layer of active material, the small thick-

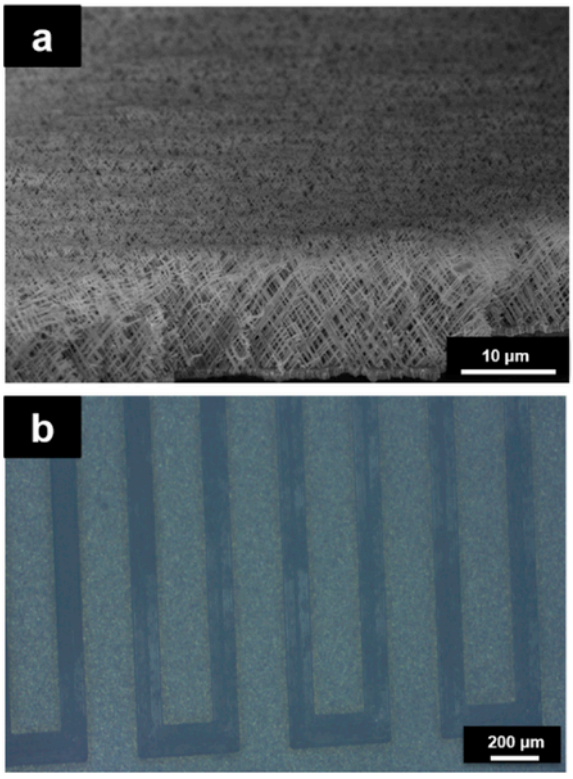

Fig. 2. (a) SEM image of as-electrodeposited Pt 3DNWN array. The height of the nanowires network is ~10 µm; (b) Optical microscope image accentuating the dimensions of the digits and interelectrode separations.

ness required for high power capabilities and facile strain accommodation upon cycling is retained, while considerably enhancing the areal capacitance of the microsupercapacitor. Furthermore, interdigitated electrodes have short interelectrode ion-transport distances, which lead to very low ohmic resistance, hence high-power capabilities, of the device. To prove the feasibility of this approach, we have fabricated and tested a symmetrical 3D-INED microsupercapacitor based on core/shell platinum/polyaniline (Pt/PANI) 3DNWN. PANI is extensively used as an active material in energy storage systems, either as cathode in (micro)batteries [42–45] or in (micro)supercapacitors [46,47]. Features such as its large capacitance due to redox pseudocapacitive charge-storage mechanism, much lower cost compared to other pseudocapacitive materials (e.g., RuO_2), and the possibility of synthesis by electroless deposition, make it a promising material for 3D microsupercapacitor applications [46,48].

2. Materials and methods

Fig. 1(a–e) shows the multi-step fabrication process of the structured electrodes based on Pt/PANI 3DNWN. The polycarbonate (PC) porous membranes with interconnected pores were fabricated by exposing a 22 µm-thick PC film to a two-step irradiation process (Fig. 1a). The topology of the membrane is defined by exposing the film to a first irradiation step at two fixed angles of – 25° and +25° with respect to the normal axis of the film plane. After rotating the PC film in the plane by 90°, the second irradiation step takes place at the same fixed angular irradiation flux to finally form a 3D nanochannel network. The diameter of the latent tracks was enlarged by following a previously reported protocol to obtain membranes with average pore diameter of 230 nm and volumetric porosity of 22% [49].

Then Pt 3DNWN were grown by electrodeposition within a 7-mm diameter PC template centred on a 1.5 cm × 1.5 cm Cr (5 nm)/Pt (100 nm)-coated quartz substrate (Fig. 1b). The ultra-thin Cr film acts to enhance the adhesion of the Pt layer onto the quartz substrate. Electrodeposition was done with a PAR 263A Potentiostat by applying −0.3 V versus a double-junction Ag/AgCl reference electrode (KCl-saturated) from a commercial Pt-DNS electrolyte (10 g Pt/l, Metakem), and a Pt strip used as counter electrode. To ensure proper adhesion of the nanowires on the substrate, electrodeposition was carried out at two temperature regimes – first at 25 °C for 1500 s, then at 50 °C until process completion. During the Pt electrodeposition process, the total charge was monitored and maintained at 10 Coulombs. Next, the Pt 3DNWN supported on the Cr/Pt-coated quartz substrate was revealed by dissolving the PC template in dichloromethane, followed by gentle rinsing with distilled water (Fig. 1c).

After fabrication of Pt 3DNWN on the Cr/Pt-coated quartz substrate, the sample was laser-patterned with an Oxford Technologies picosecond laser to form side-by-side interdigitated electrodes (Fig. 1d). A small, constant pulse rate of 1 pulse per 5 µs (i.e., frequency of 200 kHz), was used to give an ultra-precise control of surface ablation. The laser beam wavelength was 355 nm, the operating power was 3 W, the spot diameter was 10 µm, and the engraving speed was 200 mm/s. Each digit was 200 µm wide, 6 mm long and the interelectrode distance (pitch) was 100 µm. Finally, PANI was grown by electroless deposition on supported 3DNWN scaffolds to form core/shell platinum/polyaniline (Pt/PANI) 3DNWN (Fig. 1e), using a reported procedure described elsewhere [50–52]. To allow for direct comparison, Pt (100 nm)-coated quartz substrates were also functionalized with the active material, PANI films, by electroless deposition. To assure process reproducibility, all samples were thoroughly cleaned for 2 min. in a RF plasma (5 mTorr Ar, 100 W) prior to PANI growth. In the electroless deposition procedure, PANI is obtained through the polymerization of aniline on the Pt surface acting as catalyst. The process is based on spontaneous chemical reactions in acidic medium, involving reduction of dissolved oxygen as cathodic half-reaction and oxidation of aniline as anodic half-reaction at the metal/solution interface [50]. Briefly, the aniline stock reagent (99.5%, Sigma Aldrich) was first purified by filtration through a micro-column made up of alumina nanoparticles. Then, the aniline solution was prepared by mixing equimolar quantities (0.4 M) of aniline and H_2SO_4. The solution was afterwards saturated with O_2 gas by bubbling for 30 min. The electroless deposition process was carried out in a temperature-regulated double-wall glass reactor at 25 °C under continuous O_2 gas flow (kept at 0.5 sccm) for sample immersion durations ranging from 2 to 8 h. In addition, the PANI deposition process was done at 25 °C for 2 h to yield PANI thin films, and at 50 °C for 6 h to yield PANI thick films, on bare Pt substrates.

Linear sweep voltammetry was done in a three-electrode cell set-up (screen-printed electrode, Metrohm), with Pt working and counter electrodes, Ag as the pseudo-reference electrode, and 1 M $LiClO_4$/acetonitrile solution as the electrolyte. The anodic potential was scanned from 0 to +3 V, and the cathodic potential was scanned from 0 to −2 V, both at a scan rate of 10 mV/s. Cyclic voltammetry (CV) of a 2 µm-thick PANI film in 1 M $LiClO_4$/acetonitrile solution was recorded in a three-electrode cell setup, using an Ag wire pseudo-reference electrode and Pt wire counter electrode. The electrode potential was scanned from −0.2 V to 1.4 V at a rate of 10 mV/s. For both tests, all cell components were first vacuum-dried in a Haraeus Vacutherm vacuum oven for 18 h, then assembled in an Ar-filled glovebox. The tests were carried out on a BioLogic SP-300 potentiostat.

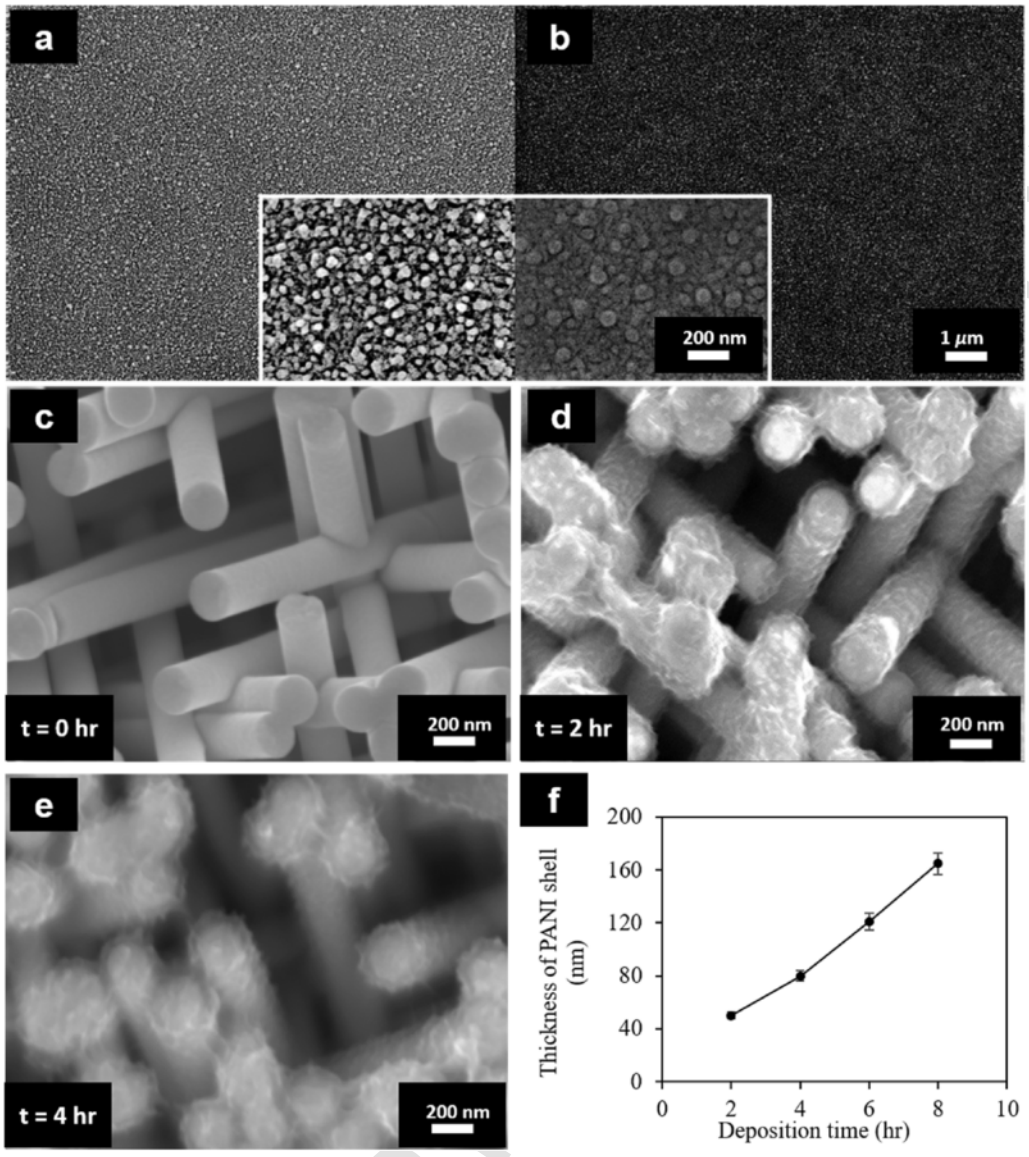

Fig. 3. Calibration of PANI growth: SEM images of (a) 2 μm-thick PANI film; (b) 50 nm-thick PANI film; SEM top-view images of Pt 3DNWN (c) before PANI deposition; (d, e) after 2 and 4 h, respectively; (f) Linear correlation of PANI shell thickness with growth time.

Morphological observation of the samples was performed using a JEOL 7600F field-emission scanning electron microscope (FE-SEM). The PANI film microsupercapacitors and 3D-INED microsupercapacitor were assembled in different kinds of cells. The thin- and thick-film electrodes were each assembled into CR2032 coin cells, while the 3D-INED microsupercapacitor was tested in a custom-made cell. Before assembling, all cell components were dried at 70 °C for 18 h in the vacuum oven. Assembling of CR2032 coin cells containing thick- and thin-film electrodes were done in an Ar-filled glovebox, using thin stainless-steel foil as electrical connectors from the PANI film to the coin cell case, two pieces of 18-mm diameter Whatmann 1823-150 glass microfiber filters as separator, and 1 M $LiClO_4$/acetonitrile as electrolyte. The acetonitrile solvent was anhydrous and the $LiClO_4$ salt was dried before use. In the case of the 3D-INED microsupercapacitor, only after assembly in the custom-made cell, drying, and placing in the glovebox was the electrolyte added and tested. The cycling tests were performed on an Arbin battery testing system model BT2043.

3. Results and discussion

Electrodeposition has been proven to be an excellent tool for filling host porous templates with metallic nanowires to a very high degree of replication of the nanopores. Fig. 2a shows a SEM image of the Pt 3DNWN after complete dissolution of the PC template. As expected, the 3DNWN scaffold exhibits a complex branching structure, imposed by the 3D nanoporous template. The Pt 3DNWN directly grown on the Cr/Pt-coated quartz substrate displays a high degree of electrical connectivity and good mechanical stability. For our purpose, the charge for Pt 3DNWN electrodeposition was set to 10 Coulombs per 0.4 cm^2 of deposition area, resulting in a nanowire array with a vertical height of about 10 μm (Fig. 2a). We note that this height is a function of the deposition area, as well as the volumetric porosity of the template (22%) and diameter of each nanowire. The diameter of each nanowire (230 nm) corresponds to the pore size of the PC template (see Fig. 3a). Fig. 2b is an optical microscope image

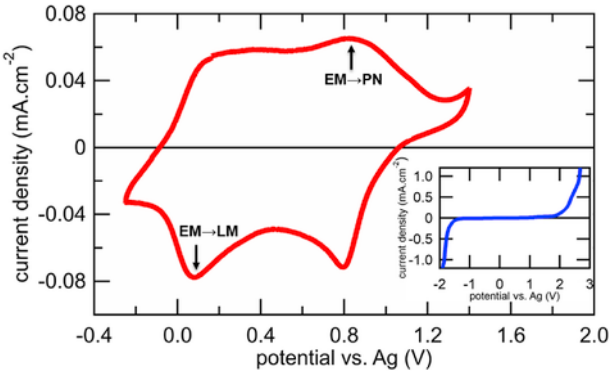

Fig. 4. Ambipolar electrochemistry/charge storage of PANI. Cyclic voltammogram of a 2 µm-thick PANI film in 1 M $LiClO_4$/acetonitrile electrolyte, highlighting both anodic and cathodic processes. Inset: the linear scan voltammogram of 1 M $LiClO_4$/acetonitrile electrolyte at the surface of a Pt working electrode. Three-electrode configuration using Ag wire as the pseudo-reference electrode and Pt wire as the counter electrode were used for both measurements at a scan rate of 10 mV/s.

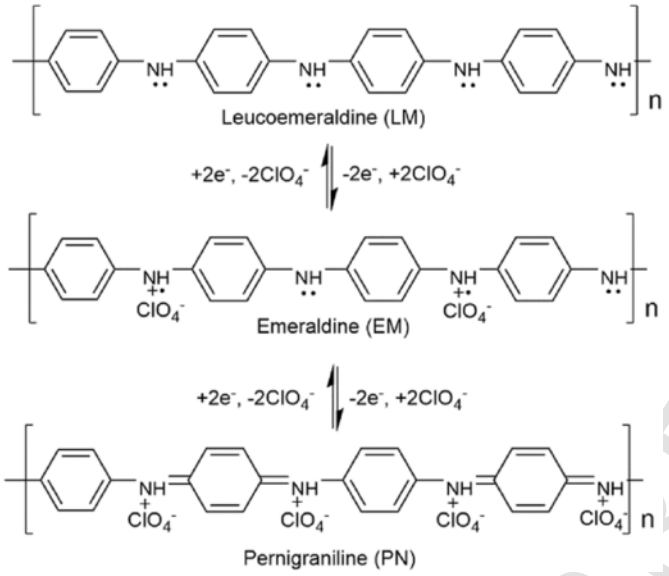

Scheme 1. Redox mechanism of polyaniline in $LiClO_4$/acetonitrile solution.

of the interdigitated electrodes after laser-patterning. It can be observed that the electrode width and interelectrode spacing are 200 µm and 100 µm, respectively. A small thickness of the substrate is also ablated during the laser patterning process to ensure electrical isolation of the electrodes to avoid short-circuiting.

PANI was deposited on planar Pt substrates at 50 °C for 6 h to yield PANI thick films, and at 25 °C for 2 h to yield PANI thin films. Fig. 3a and b show the SEM images of the deposited thick and thin films, respectively. The observed morphologies of both cases are similar. As the magnified images show (inset of Fig. 3a and b), they are homogenous, dense, and well adhered onto the Pt substrate, in agreement with the literature [50,53]. The Pt 3DNWN was also functionalized by the electroless deposition procedure to form a core/shell (Pt/PANI) structure, as shown in Fig. 3c–e. All depositions on the Pt 3DNWN scaffolds were done at 25 °C for 2–8 h. PANI can be seen to conformally coat each nanowire. The thickness of the PANI shell on Pt 3DNWN was found to be between 50 nm and 160 nm by varying the deposition time between 2 h and 8 h, as shown in Fig. 3f. In Fig. 3e, we see that the surface of the scaffold structure appears more blurred after longer deposition time, due to the increasing thickness of the PANI layer.

The PANI shell of the core/shell 3DNWN used for 3D-INED microsupercapacitor was 50-nm thick (see Fig. 3d). This thickness was used to ensure short diffusion paths for ions and improved electronic charge transfer during cycling to enhance active material utilization and power capabilities. The PANI mass loading on the Pt 3DNWN was ~0.34 mg/cm^2. The thickness of the thick film electrodes was 2 µm, corresponding to similar PANI mass loading (~0.28 mg/cm^2). However, because in the 3D-INED configuration, each electrode occupies one-third of the total surface area, the active PANI mass on each electrode is 0.04 mg, while the active mass on each thick-film electrode is 0.23 mg. To compare with the 3D-INED microsupercapacitor, the thin-film microsupercapacitor had the same PANI thickness (50 nm) as the thickness of the PANI shell in the core-shell structure, a mass of ~0.006 mg.

The electroless deposition process used for PANI synthesis restricts the choice of current collector to Pt; hence, there is the need to ascertain the suitability of Pt as current collector in the fabricated devices. The potential range within which the electrolyte (1 M $LiClO_4$/acetonitrile solution) is stable in the presence of Pt, i.e., the electrochemical stability window, was determined by linear sweep voltammetry (LSV), using Pt wire as the working electrode, Ag wire as pseudo-reference electrode, and another Pt wire as the counter electrode, all assembled and tested in an Ar-filled glovebox. The inset of Fig. 4 shows the result of the LSV; taking the conventional cut-off current density of ±1 mA/cm^2, the stability window of the electrolyte is seen to be ~4.4 V. Fig. 4 shows the cyclic voltammogram of 2 µm-thick PANI film, tested in a three-electrode setup, using Ag wire as pseudo-reference electrode and Pt wire as counter electrode. It shows that PANI redox reactions occur well within the stability window of the electrolyte, confirming the suitability of Pt as the current collector.

PANI is a conducting polymer with three main redox states – leucoemeraldine (LM), emeraldine (EM), and pernigraniline (PN) – depending on the fraction of the benzenoid and quinoid states in the overall structure [54,55]. PANI derived by the electroless deposition process in this work is in the EM-salt state, the mid-redox state; thus, its oxidation leads to the PN state, while reduction leads to the LM state. The cyclic voltammogram of PANI (Fig. 4) shows two distinct pairs of anodic and cathodic peaks, whose potentials correspond to transitions from one redox state to another. The presence of these successive redox processes, and the (almost) mirror image with respect to the potential axis at zero current, in the scanned potential window, is characteristic of charge storage by fast and reversible faradaic processes at (or close) to PANI surface, a charge-storage mechanism formally defined as pseudocapacitive [48,56]. Consistent with reports in other works [57–60], the potential difference between the EM-PN peak and LM-EM peak is ~0.7 V, implying that the voltage of a symmetrical (PANI/PANI) supercapacitor will be of the order of 0.7 V.

Three symmetrical PANI/PANI microsupercapacitor configurations were fabricated and tested – 3D-INED microsupercapacitor (3D-INED), 2 µm-thick film microsupercapacitor (thick-film), and 50 nm-thick film microsupercapacitor. (thin-film). Scheme 1 shows the mechanism of PANI (dis)charging. Each electrode is initially in the EM-salt state. By applying an oxidizing current to one electrode (i.e., charging, causing reduction of the other electrode), the electrode is oxidized to the PN state, while the other is reduced to the LM state, which results in a potential difference between the electrodes [61]. Both electrodes return to the EM-salt state after discharge. Charge storage in PANI is well-known to be by electrochemical *p*-doping, in which the application of a positive current (during device charge, for

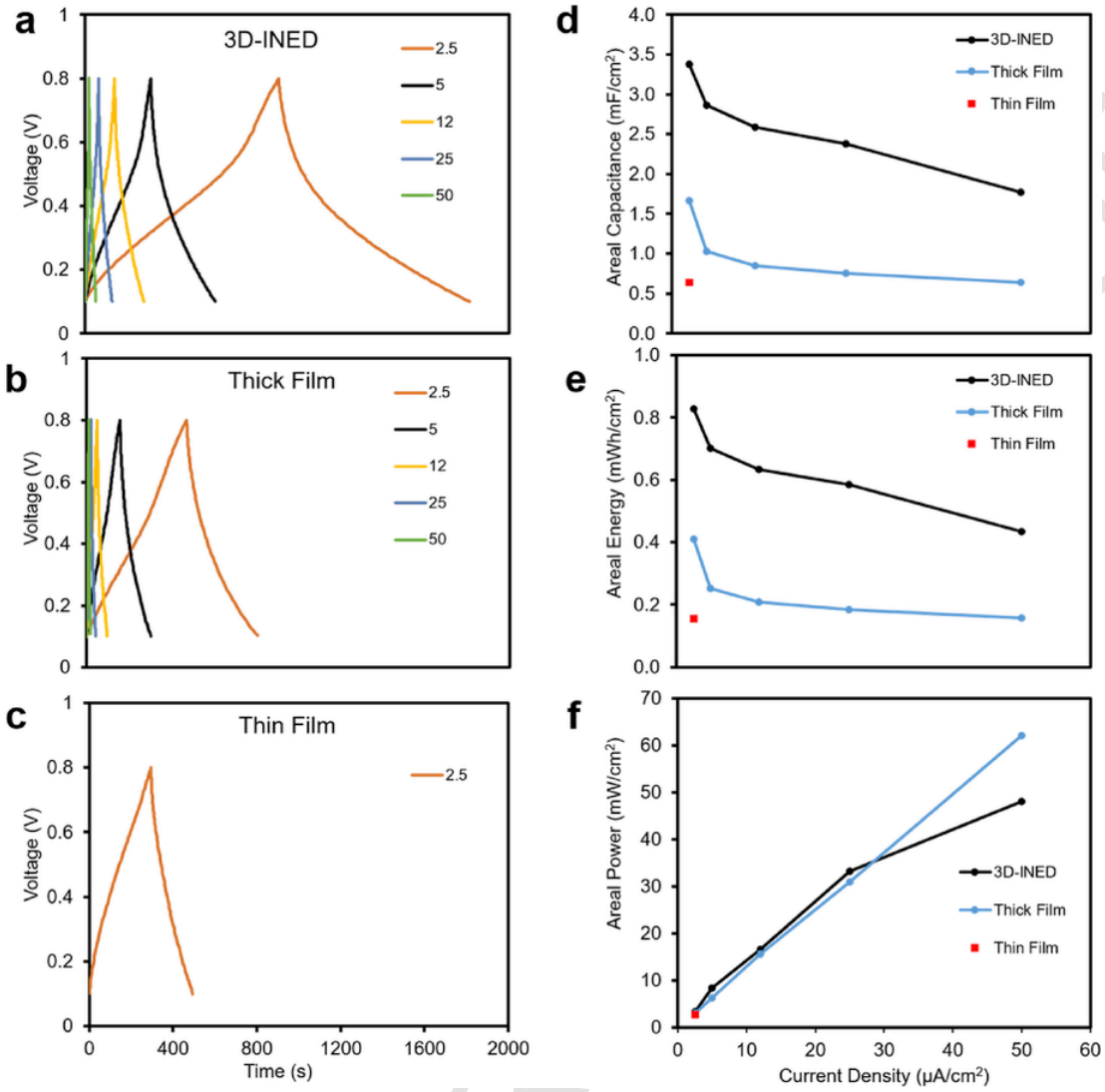

Fig. 5. Performance of microsupercapacitors: Galvanostatic charge-discharge curves for the (a) 3D-INED microsupercapacitor, (b) Thick-film microsupercapacitor, and (c) Thin-film microsupercapacitor, at different current densities (μA/cm^2). Evolution of the (d) Areal capacitance, (e) Areal energy, and (f) Areal power, as a function of current density.

instance) causes electron abstraction through the external circuit, leading to the incorporation of anions for charge balance [62].

Fig. 5a–c show the typical galvanostatic charge/discharge curves for the 3D-INED, thick-film, and thin-film, symmetrical microsupercapacitors, respectively, cycled between 0.1 and 0.8 V at current densities from 2.5 to 50 μA/cm^2. For devices in the stacked configuration (i.e., the thin- and thick-film microsupercapacitors), the current densities are based on the active surface area of individual electrodes (0.8 cm^2), while the total surface area occupied by both electrodes and the interelectrode spacing (0.4 cm^2) is used for the interdigitated configuration. These values correspond to the devices' footprint area. The very small active material mass of the thin-film device limited the cycling current to only 2.5 μA/cm^2. The triangular-shaped charge/discharge curves for the microsupercapacitors indicate the pseudocapacitive nature of PANI [56]. It can also be seen that the charge and discharge times, which correspond to the stored and delivered capacities, respectively, is highest at the lowest current density. This is due to increased active material utilization when cycling at lower current densities.

Since microsupercapacitors are to be integrated on microscale devices, which have very limited footprint area, it is more appropriate to present the performance metrics of microsupercapacitors on the basis of their footprint area [4,11]. These metrics were calculated from the charge-discharge curves according to Equations (1)–(3) [63]:

$$C_s = \frac{It}{A\Delta V} = Q/A\Delta V \quad (1)$$

$$W_s = \frac{C_s(\Delta V)^2}{3600} \quad (2)$$

$$P_s = \frac{W_s}{\Delta t} \quad (3)$$

where C_s is the areal capacitance (mF/cm^2), Q is the total charge (mAh) delivered over the discharge time of Δt (s) in the potential

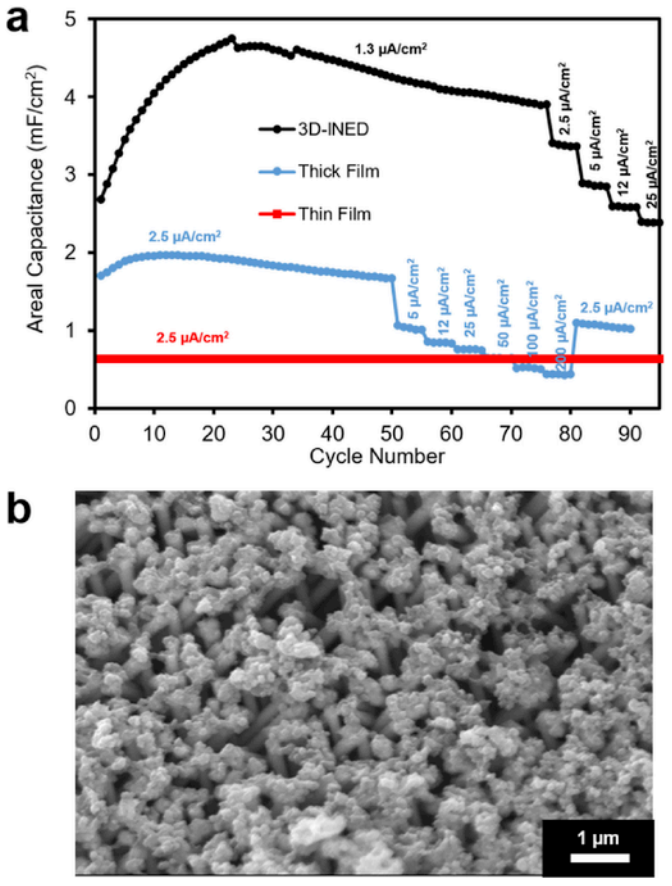

Fig. 6. (a) Comparative areal capacitance and cycling performances of the 3D-INED, thick-film, and thin-film symmetrical PANI/PANI microsupercapacitors at various current densities; (b) Post-cycling SEM image of the $Pt_{core}/PANI_{shell}$ (50 nm) 3DNWN after 130 cycles.

window of ΔV (V), A (cm^2) is the device footprint area, W_s is the areal energy (mWh/cm^2), and P_s is the areal power (mW/cm^2).

Fig. 5d–f show the calculated areal capacitance, energy and power of the microsupercapacitors at different current densities. It can be seen that at the lowest current density, the 3D-INED microsupercapacitor has areal capacitance and energy 2 times more than the thick-film, and 7 times more than the thin-film, microsupercapacitors. To have a clearer view of the improvements conferred by the 3D-INED architecture, consider, as we have seen, that each electrode has a mass of 0.04 mg, 0.23 mg, and 0.006 mg, for the 3D-INED, thick-film, and thin-film, microsupercapacitors, respectively. Thus, the areal capacitances per active mass of a single electrode are similar for the 3D-INED and thin-film microsupercapacitors (~100mF/cm^2g), while the thick-film microsupercapacitor attains less than 10% of this value. This result is ascribed to a combined influence of increased PANI utilization, because of its nanometric thickness on the 3DNWN and thin film (i.e. shorter diffusion length), and a higher contribution of the double-layer capacitance to the observed pseudocapacitance, because of active surface area enhancement of more than 30 times by the 3DNWN. Furthermore, Fig. 5d shows that the improved areal capacitance and energy of the 3D-INED microsupercapacitor did not result at the expense of its areal power. In fact, at low current densities (<30 μA/cm^2), the 3D-INED supercapacitor exhibits higher power capabilities.

The rate capabilities of the microsupercapacitors are shown in Fig. 6. In all cases, an initial increase in the discharge capacitances can be observed, evidence of enhanced material utilization of the electrode materials with cycling. Subsequently, while the thin-film microsupercapacitor holds a constant discharge capacitance of 0.7 mF/cm^2 throughout its cycle life (more than 800 cycles), the discharge capacitance of the thick-film and 3D-INED microsupercapacitors begin to slightly fade after reaching maximum values on about the 30th cycle. All the devices exhibit good rate capabilities, with very slight capacitance fade with increase in cycling current density. Overall, the thin-film microsupercapacitor exhibited the best cycle life, followed by the 3D-INED microsupercapacitor. Evidenced by Fig. 6b, the PANI shell, while slightly deformed, still remains on the Pt 3D-NWN scaffold after more than 130 cycles, which explains its long cycle life. The thick-film microsupercapacitor exhibited the worst cycle life, and we attribute this to the fact that thicker films do not undergo size changes as facilely as thin films during cycling.

4. Conclusion

The inability of state-of-the-art stacked microsupercapacitors to simultaneously meet the performance and size requirements for constantly miniaturizing autonomous microscale devices has triggered an extensive interest in looking for microsupercapacitor architectures capable of fulfilling these requirements. Whereas some progress has been reported for 3D microsupercapacitors, the fabrication processes for these microsupercapacitors suffer from important drawbacks. We have shown in this work a simple and versatile technique based on laser-patterning of substrate-supported metallic 3D interconnected nanowire network (3DNWN) that act as 3D scaffolds and current collectors for the electrode active materials.

Electrodeposition and electroless deposition methods have also been identified as key tools for the 3D interdigitated nanowire electrode design (3D-INED), because they satisfy the process requirements of, importantly, being selective, and able to form conformal active material deposits on complicated 3D geometries, in addition to being low-cost processes. The PANI/PANI symmetrical microsupercapacitor is not presented as an ideal microsupercapacitor, because it has a small voltage (0.7 V). it is instead presented as a proof of the symmetrical 3D-INED concept. Although having 5 times less material than the thick-film stacked configuration, the 3D-INED configuration shows a footprint areal capacitance enhancement of more than twice for only 10 μm-high interconnected nanowires, in addition to higher power capabilities at current densities less than 30 μA/cm^2. Therefore, the 3D-INED configuration increases the areal capacitance/energy of microsupercapacitors without penalizing the power capabilities of the stacked configuration, despite having much smaller active material. We ascribe this improvement to the possibility of increasing the active material while retaining the nanometric thickness required for high power capabilities, and increased active material utilization.

It has been shown that 3DNWN with height of 20 μm and diameter of 40 nm, an aspect ratio of 500, is attainable [29]; therefore, the performance of the 3D-INED microsupercapacitor can be vastly improved by varying the thickness of the active material, increasing the height of the nanowires and/or reducing their average diameter, as well as by ultimately changing the device chemistry. The promising results obtained in this work open the pathway towards low-cost processing and manufacturing of integrated microsupercapacitors and microbatteries for modern autonomous microscale electronic and optoelectronic devices.

Appendix A. Supplementary data

Supplementary data to this article can be found online at https://doi.org/10.1016/j.ensm.2019.05.025.

References

[1] A. Raj, D. Steingart, Review—power sources for the internet of things, J. Electrochem. Soc. 165 (2018) B3130–B3136, https://doi.org/10.1149/2.0181808jes.

[2] D. Bandyopadhyay, J. Sen, Internet of things: applications and challenges in technology and standardization, Wireless Pers. Commun. 58 (2011) 49–69, https://doi.org/10.1007/s11277-011-0288-5.

[3] K.A. Cook-Chennault, N. Thambi, A.M. Sastry, Powering MEMS portable devices - a review of non-regenerative and regenerative power supply systems with special emphasis on piezoelectric energy harvesting systems, Smart Mater. Struct. 17 (2008) https://doi.org/10.1088/0964-1726/17/4/043001.

[4] N.A. Kyeremateng, T. Brousse, D. Pech, Microsupercapacitors as miniaturized energy-storage components for on-chip electronics, Nat. Nanotechnol. 12 (2017) 7–15, https://doi.org/10.1038/nnano.2016.196.

[5] R. Huggins, Supercapacitors and electrochemical pulse sources, Solid State Ionics 134 (2000) 179–195, https://doi.org/10.1016/S0167-2738(00)00725-6.

[6] J.H. Lim, D.J. Choi, H.-K. Kim, W Il Cho, Y.S. Yoon, Thin film supercapacitors using a sputtered RuO[sub 2] electrode, J. Electrochem. Soc. 148 (2002) A275, https://doi.org/10.1149/1.1350666.

[7] Y.S. Yoon, W.I. Cho, J.H. Lim, D.J. Choi, Solid-state thin-film supercapacitor with ruthenium oxide and solid electrolyte thin films, J. Power Sources 101 (2001) 126–129.

[8] D. Pech, M. Brunet, T.M. Dinh, K. Armstrong, J. Gaudet, D. Guay, Influence of the configuration in planar interdigitated electrochemical micro-capacitors, J. Power Sources 230 (2013) 230–235, https://doi.org/10.1016/j.jpowsour.2012.12.039.

[9] M. Beidaghi, Y. Gogotsi, Capacitive energy storage in micro-scale devices: recent advances in design and fabrication of micro-supercapacitors, Energy Environ. Sci. 7 (2014) 867–884, https://doi.org/10.1039/c3ee43526a.

[10] A. Ghosh, Y.H. Lee, Carbon-based electrochemical capacitors, ChemSusChem 5 (2012) 480–499, https://doi.org/10.1002/cssc.201100645.

[11] D.R. Rolison, J.W. Long, J.C. Lytle, A.E. Fischer, C.P. Rhodes, T.M. McEvoy, et al., Multifunctional 3D nanoarchitectures for energy storage and conversion, Chem. Soc. Rev. 38 (2009) 226–252, https://doi.org/10.1039/B801151F.

[12] A. Vlad, N. Singh, C. Galande, P.M. Ajayan, Design considerations for unconventional electrochemical energy storage architectures, Adv. Energy Mater. 5 (2015) https://doi.org/10.1002/aenm.201402115.

[13] T.S. Arthur, D.J. Bates, N. Cirigliano, D.C. Johnson, P. Malati, J.M. Mosby, et al., Three-dimensional electrodes and battery architectures, MRS Bull. 36 (2011) 523–531, https://doi.org/10.1557/mrs.2011.156.

[14] J.W. Long, B. Dunn, D.R. Rolison, H.S. White, Three-dimensional battery architectures, Chem. Rev. 104 (2004) 4463–4492, https://doi.org/10.1021/cr0207401.

[15] P.H.L. Notten, F. Roozeboom, R.A.H. Niessen, L. Baggetto, 3-D integrated all-solid-state rechargeable batteries, Adv. Mater. 19 (2007) 4564–4567, https://doi.org/10.1002/adma.200702398.

[16] C. Meng, J. Maeng, S.W.M. John, P.P. Irazoqui, Ultrasmall integrated 3d micro-supercapacitors solve energy storage for miniature devices, Adv. Energy Mater. 4 (2014) 1–7, https://doi.org/10.1002/aenm.201301269.

[17] A. Ferris, S. Garbarino, D. Guay, D. Pech, 3D RuO2 microsupercapacitors with remarkable areal energy, Adv. Mater. 27 (2015) 6625–6629, https://doi.org/10.1002/adma.201503054.

[18] C. Shen, S. Xu, Y. Xie, M. Sanghadasa, X. Wang, L. Lin, A review of on-chip micro supercapacitors for integrated self-powering systems, J. Microelectromech. Syst. 26 (2017) 949–965, https://doi.org/10.1109/JMEMS.2017.2723018.

[19] Z. Huang, B. Yuan, All-solid-state pseudocapacitive micro-supercapacitors from laser-treated polymer derivatives, 29 (2018) 596–598.

[20] W. Sun, R. Zheng, X. Chen, Symmetric redox supercapacitor based on micro-fabrication with three-dimensional polypyrrole electrodes, J. Power Sources 195 (2010) 7120–7125, https://doi.org/10.1016/j.jpowsour.2010.05.012.

[21] M. Beidaghi, C. Wang, Micro-supercapacitors based on three dimensional interdigital polypyrrole/C-MEMS electrodes, Electrochim. Acta 56 (2011) 9508–9514, https://doi.org/10.1016/j.electacta.2011.08.054.

[22] W. Wang, M. Tian, A. Abdulagatov, Three-dimensional Ni/TiO2 nanowire network for high areal capacity lithium-ion microbattery applications, Nano Lett. (2012) 655–660.

[23] C. Wei, H. Pang, B. Zhang, Q. Lu, S. Liang, F. Gao, Two-dimensional β-MnO2 nanowire network with enhanced electrochemical capacitance, Sci. Rep. 3 (2013) 2193, https://doi.org/10.1038/srep02193.

[24] A. Vlad, V.-A. Antohe, J.M. Martinez-Huerta, E. Ferain, J.-F. Gohy, L. Piraux, Three-dimensional interconnected Ni_{core} –NiO_{shell} nanowire networks for lithium microbattery architectures, J. Mater. Chem. A 4 (2016) 1603–1607, https://doi.org/10.1039/C5TA10639G.

[25] O.S. Kwon, S.J. Park, H. Yoon, J. Jang, Highly sensitive and selective chemiresistive sensors based on multidimensional polypyrrole nanotubes, Chem. Commun. 48 (2012) 10526, https://doi.org/10.1039/c2cc35307e.

[26] L. Piraux, V.A. Antohe, E. Ferain, D. Lahem, Self-supported three-dimensionally interconnected polypyrrole nanotubes and nanowires for highly sensitive chemiresistive gas sensing, RSC Adv. 6 (2016) https://doi.org/10.1039/c6ra03439j, 21808–13.

[27] I. Paulowicz, V. Hrkac, S. Kaps, V. Cretu, O. Lupan, T. Braniste, et al., Three-dimensional SnO2 nanowire networks for multifunctional applications: from high-temperature stretchable ceramics to ultraresponsive sensors, Adv. Electron Mater. 1 (2015) 1500081, https://doi.org/10.1002/aelm.201500081.

[28] E. Araujo, A. Encinas, Y. Velázquez-Galván, J.M. Martínez-Huerta, G. Hamoir, E. Ferain, et al., Artificially modified magnetic anisotropy in interconnected nanowire networks, Nanoscale 7 (2015) 1485–1490, https://doi.org/10.1039/C4NR04800H.

[29] T. Da Câmara Santa Clara Gomes, J. De La Torre Medina, Y.G. Velázquez-Galván, J.M. Martínez-Huerta, A. Encinas, L. Piraux, Interplay between the magnetic and magneto-transport properties of 3D interconnected nanowire networks, J. Appl. Phys. 120 (2016) https://doi.org/10.1063/1.4959249.

[30] T. da Câmara Santa Clara Gomes, J. De La Torre Medina, M. Lemaitre, L. Piraux, Magnetic and magnetoresistive properties of 3D interconnected NiCo nanowire networks, Nanoscale Res. Lett. 11 (2016) 466, https://doi.org/10.1186/s11671-016-1679-z.

[31] T. da Câmara Santa Clara Gomes, F. Abreu Araujo, L. Piraux, Making flexible spin caloritronic devices with interconnected nanowire networks, Sci. Adv. 5 (2019)eaav2782https://doi.org/10.1126/sciadv.aav2782.

[32] M. Rauber, I. Alber, S. Muöller, R. Neumann, O. Picht, C. Roth, et al., Highly-ordered supportless three-dimensional nanowire networks with tunable complexity and interwire connectivity for device integration, Nano Lett. 11 (2011) 2304–2310, https://doi.org/10.1021/nl2005516.

[33] M.R.J. Scherer, U. Steiner, Efficient electrochromic devices made from 3D nanotubular gyroid networks, Nano Lett. 13 (2013) 3005–3010, https://doi.org/10.1021/nl303833h.

[34] E.J.W. Crossland, M. Kamperman, M. Nedelcu, C. Ducati, U. Wiesner, D.-M. Smilgies, et al., A bicontinuous double gyroid hybrid solar cell, Nano Lett. 9 (2009) 2807–2812, https://doi.org/10.1021/nl803174p.

[35] S. Wang, L.-P. Xu, H.-W. Liang, S.-H. Yu, Y. Wen, S. Wang, et al., Self-interconnecting Pt nanowire network electrode for electrochemical amperometric biosensor, Nanoscale 7 (2015) 11460–11467, https://doi.org/10.1039/C5NR02526E.

[36] S. Rahong, T. Yasui, T. Yanagida, K. Nagashima, M. Kanai, G. Meng, et al., Three-dimensional nanowire structures for ultra-fast separation of DNA, protein and RNA molecules, Sci. Rep. 5 (2015) 10584, https://doi.org/10.1038/srep10584.

[37] S. Rahong, T. Yasui, T. Yanagida, K. Nagashima, M. Kanai, A. Klamchuen, et al., Ultrafast and wide range analysis of DNA molecules using rigid network structure of solid nanowires, Sci. Rep. 4 (2015) 5252, https://doi.org/10.1038/srep05252.

[38] S. Xiong, C. Yuan, X. Zhang, Y. Qian, Mesoporous NiO with various hierarchical nanostructures by quasi-nanotubes/nanowires/nanorodsself-assembly: controllable preparation and application in supercapacitors, CrystEngComm 13 (2011) 626–632, https://doi.org/10.1039/C002610G.

[39] Donghai Wang, Hans Peter Jakobson, Rong Kou, Jing Tang, Robert Z. Fineman, Donghong Yu, et al., Metal and Semiconductor Nanowire Network Thin Films with Hierarchical Pore Structures, 2006https://doi.org/10.1021/CM052216B.

[40] M. Tian, W. Wang, Y. Wei, R. Yang, Stable high areal capacity lithium-ion battery anodes based on three-dimensional Ni-Sn nanowire networks, J. Power Sources 211 (2012) 46–51, https://doi.org/10.1016/j.jpowsour.2012.03.084.

[41] J. Martín, M. Martín-González, J. Francisco Fernández, O. Caballero-Calero, Ordered three-dimensional interconnected nanoarchitectures in anodic porous alumina, Nat. Commun. 5 (2014) 5130, https://doi.org/10.1038/ncomms6130.

[42] Q. Ju, Y. Shi, J. Kan, Performance study of magnesium-polyaniline rechargeable battery in 1-ethyl-3-methylimidazolium ethyl sulfate electrolyte, Synth. Met. 178 (2013) 27–33, https://doi.org/10.1016/j.synthmet.2013.06.016.

[43] B.Z. Jugović, T.L. Trišović, J. Stevanović, M. Maksimović, B.N. Grgur, Novel electrolyte for zinc-polyaniline batteries, J. Power Sources 160 (2006) 1447–1450, https://doi.org/10.1016/j.jpowsour.2006.02.096.

[44] S.R. Gowda, A. Leela, M. Reddy, P.M. Ajayan, 3D Nanoporous Current Collectors for Advanced Thin Film Microbatteries, 2012, 2012.

[45] A.G. Macdiarmid, J.C. Chiang, A.F. Richter, A.J. Epstein, Polyaniline: a new concept in conducting polymers, Synth. Met. 18 (1987) 285–290, https://doi.org/10.1016/0379-6779(87)90893-9.
[46] K.S. Ryu, K.M. Kim, N.G. Park, Y.J. Park, S.H. Chang, Symmetric redox supercapacitor with conducting polyaniline electrodes, J. Power Sources 103 (2002) 305–309, https://doi.org/10.1016/S0378-7753(01)00862-X.
[47] A. Eftekhari, L. Li, Y. Yang, Polyaniline supercapacitors, J. Power Sources 347 (2017) 86–107, https://doi.org/10.1016/j.jpowsour.2017.02.054.
[48] B.E. Conway, Transition from "supercapacitor" to "battery" behavior in electrochemical energy storage, J. Electrochem. Soc. 138 (2006) 1539, https://doi.org/10.1149/1.2085829.
[49] E. Ferain, R. Legras, Track-etch templates designed for micro- and nanofabrication, Nucl. Instrum. Methods Phys. Res. Sect. B Beam Interact. Mater. Atoms 208 (2003) 115–122, https://doi.org/10.1016/S0168-583X(03)00637-2.
[50] A. Attout, S. Yunus, P. Bertrand, Electroless deposition of polyaniline: synthesis and characterization, Surf. Interface Anal. 40 (2008) 657–660, https://doi.org/10.1002/sia.2702.
[51] A. Vlad, C.A. Dutu, P. Jedrasik, U. Södervall, J.F. Gohy, S. Melinte, Vertical single nanowire devices based on conducting polymers, Nanotechnology 23 (2012) https://doi.org/10.1088/0957-4484/23/2/025302.
[52] V.A. Antohe, A. Radu, M. Mátfí-Tempfli, A. Attout, S. Yunus, P. Bertrand, et al., Nanowire-templated microelectrodes for high-sensitivity pH detection, Appl. Phys. Lett. 94 (2009) 1–4, https://doi.org/10.1063/1.3089227.
[53] C.G. Wu, H.T. Hsiao, Y.R. Yeh, Electroless surface polymerization of polyaniline films on aniline primed ITO electrodes: a simple method to fabricate good modified anodes for polymeric light emitting diodes, J. Mater. Chem. 11 (2001) 2288–2293, https://doi.org/10.1039/b102084f.
[54] J.G. Masters, Y. Sun, A.G. MacDiarmid, A.J. Epstein, Polyaniline: allowed oxidation states, Synth. Met. 41 (1991) 715–718, https://doi.org/10.1016/0379-6779(91)91166-8.
[55] A.G. MacDiarmid, A.J. Epstein, Polyanilines: a novel class of conducting polymers, Faraday Discuss. Chem. Soc. 88 (1989) 317, https://doi.org/10.1039/dc9898800317.
[56] B.E. Conway, Electrochemical Supercapacitors: Scientific Fundamentals and Technological Applications, Kluwer Academic/Plenum Publishers, New York, 1999.
[57] B. Garcia, F. Fusalba, D. Bélanger, Electrochemical characterization in nonaqueous electrolyte of polyaniline electrochemically prepared from aqueous media, Can. J. Chem. 75 (1997) 1536–1541, https://doi.org/10.1139/v97-185.
[58] T. Osaka, T. Nakajima, K. Naoi, B.B. Owens, Electroactive polyaniline film deposited from nonaqueous organic media, J. Electrochem. Soc. 137 (1990) 2139, https://doi.org/10.1149/1.2086899.
[59] A. Watanabe, K. Mori, M. Mikuni, Y. Nakamura, M. Matsuda, Comparative study of the redox reactions of polyaniline films in aqueous and nonaqueous solutions, Macromolecules 22 (1989) 3323–3327.
[60] H. Daifuku, T. Kawagoe, A study of the redox reaction mechanisms of polyaniline using a quartz crystal microbalance, 214 (1989) 1989, https://doi.org/10.1016/0022-0728(89)87054-8.
[61] R. De Surville, M. Jozefowicz, L.T. Yu, J. Pepichon, R. Buvet, Electrochemical chains using protolytic organic semiconductors, Electrochim. Acta 13 (1968) 1451–1458, https://doi.org/10.1016/0013-4686(68)80071-4.
[62] A. Rudge, J. Davey, I. Raistrick, J.P. Ferraris, Conducting Polymers as Active Materials Electrochemical Capacitors, vol. 47, 1994.
[63] H.B. Hu, Z.B. Pei, H.J. Fan, C.H. Ye, 3D interdigital Au/MnO2/Au stacked hybrid electrodes for on-chip microsupercapacitors, Small 12 (2016) 3059–3069, https://doi.org/10.1002/smll.201503527.